Article

Synthesis and Characterization of Multifunctional Fluorescent-Magnetic Platinum Nanoclusters

Shin-ichi Tanaka,* Kohei Yamagami, Kazuhisa Sato, Hidehiro Yasuda, Hirohiko Niioka, and Hiroki Wadati

Cite This: ACS Omega 2024, 9, 50349−50356

Read Online

ACCESS | Metrics & More | Article Recommendations | Supporting Information

ABSTRACT: There is great interest in the development of new multifunctional fluorescent-magnetic nanomaterials for use as multimodal diagnostic imaging probes and site-specific drug delivery tools. Metal nanoclusters (NCs) have been reported to possess either fluorescent or magnetic properties, but not both. In this paper, we report the synthesis and characterization of multifunctional fluorescent-magnetic Pt NCs. Our synthesized NCs (0.8 ± 0.2 nm in diameter) exhibit both bright red fluorescence (excitation: 535 nm, emission: 620 nm) and ferromagnetic behavior with hysteresis, which represents a

noteworthy and significant advance in the development of Pt NCs. Our findings suggest the potential of our NCs to be applied in multimodal fluorescent-magnetic nanomaterials for biomedical applications.
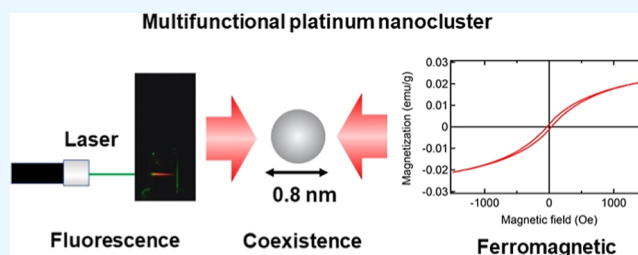
1. INTRODUCTION

Multimodal fluorescent-magnetic-based nanomaterials deserve particular attention, as they can be used as diagnostic and drug delivery tools. For example, magnetic resonance imaging (MRI)/fluorescence imaging hybrids are assumed to have clinical potential because of the combination of the superior anatomical detail achieved via MRI and the sensitive molecular information achieved via fluorescence imaging. In drug delivery systems, such nanocomposites can potentially be applied as nanoprobes. These materials can be delivered to a site of interest by using external magnetic fields, and their dynamics also allow tracking of this delivery with fluorescence imaging. However, as each imaging modality uses different contrast agents with distinctive chemical compositions, sizes, solubilities, and pharmacokinetic profiles, it is difficult to employ a cocktail approach by using a mixture of various contrast agents together in a single dose to achieve spatiotemporal consistency for all imaging/application techniques. Therefore, a single probe that integrates dual or multiple properties is preferred for dual- or multimodality biomedical applications.

In recent years, multifunctional nanomaterials for biomedical applications have been synthesized by labeling magnetic nanoparticles with fluorescent dyes[1−4] or hybridizing luminescent semiconductor quantum dots (QDs) with magnetic compounds, such as gadolinium complexes.[5−7] However, these nanomaterials are larger and often disturb the biological function in a living cell or within an organism. In addition, these nanocomposites exhibit low photostability due to photobleaching of fluorescence dyes and exhibit intrinsic toxicity because of the presence of heavy metals. Therefore,

they are unsuitable for the fabrication of stable, multifunctional nanodevices for application in *in vivo* multimodal imaging and site-specific drug delivery systems.

1.1. Ultrasmall Metallic Nanoclusters Offer Significant Potential for Overcoming the Existing Challenges in the Development of Multimodal Imaging Probes. Metallic NCs are composed of several to approximately one hundred atoms (<1 nm) and have sizes comparable to the Fermi wavelength, resulting in molecular-like behavior, including discrete electronic states and size-dependent fluorescence. In the last two decades, metallic NCs, such as gold (Au),[8−16] silver (Ag),[17−19] copper (Cu),[20,21] palladium (Pd)[22] and platinum (Pt),[23−30] have been intensely investigated for their unique optical,[8−12,16−25] chiral,[13,14] magnetic[15,26] and catalytic[20,22,27−30] properties and potential to be used in a wide range of applications, including catalysis, photonics, optics, nanoelectronics, sensing[16] and biomedical imaging.

In previous studies, we and other groups developed water-soluble Pt NCs that exhibited fluorescence from the blue to the near-infrared region[23−25] and higher biocompatibilities than other metal NCs, except for gold. The synthesis of Pt NCs was achieved through our previously reported method,[25] whereby
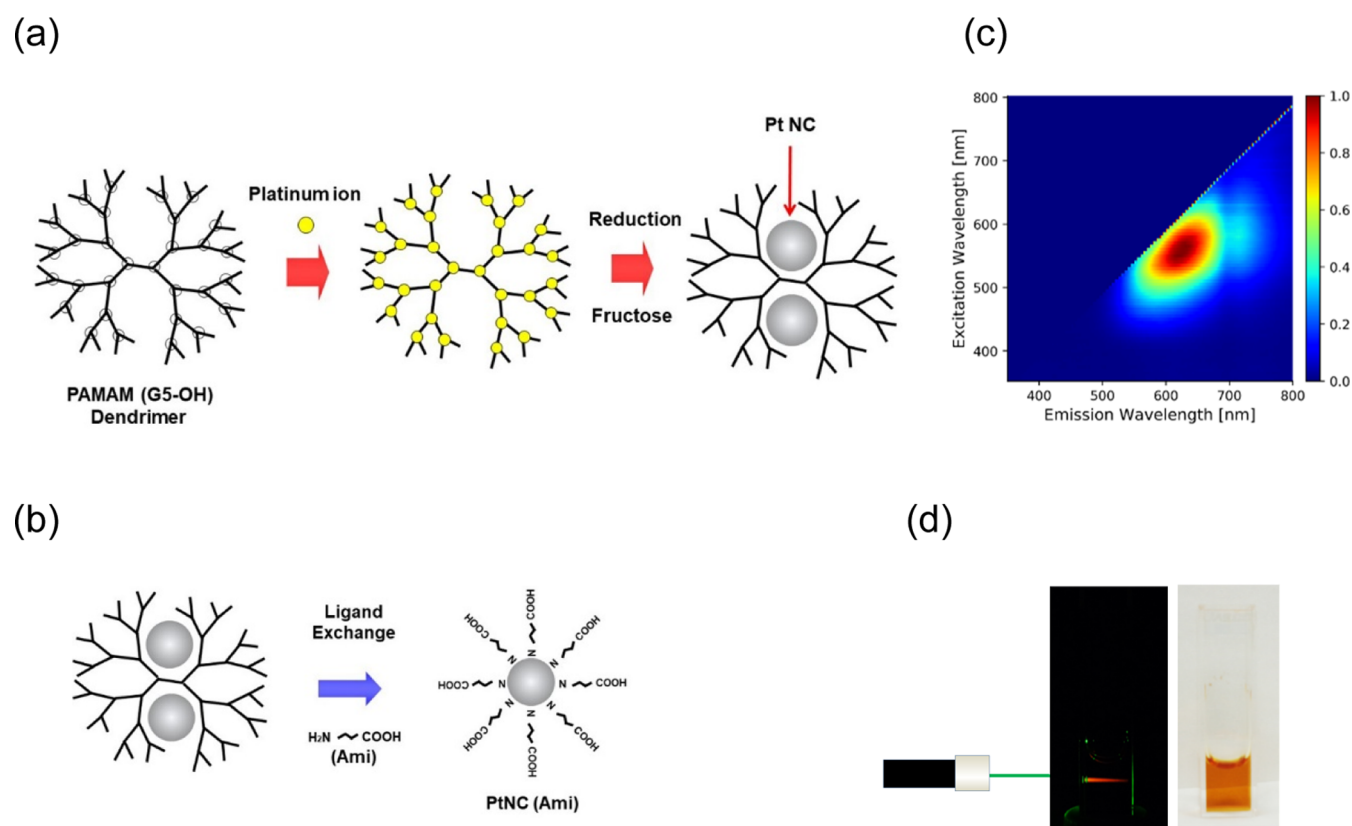
Figure 1. Synthesis process and red-emission properties of Pt NCs. (a) The Pt NCs were synthesized via our previously reported method.[25] Schematic illustration of our facile two-step Pt NC synthesis process which involves coordination bond formation between PAMAM dendrimers and Pt ions during pre-equilibration and subsequent reduction with a large amount of fructose. White circles indicate the tertiary amine branches of the PAMAM dendrimers, which can trap Pt ions by forming coordination bonds. (b) Schematic illustration of ligand exchange which was performed with 4-amino butyric acid (Ami) after the synthesis process illustrated in Figure 1a. (c) Excitation/emission matrix spectra revealing that [PtNC(Ami)] exhibited red fluorescence (620 nm) at 535 nm excitation. The bar chart next to the graph indicates the contour intervals of the normalized fluorescence intensity. In previous work, Pt NCs embedded in PAMAM (G5−OH) dendrimers also displayed red fluorescence with a maximum excitation/emission wavelength of 535/630 nm.[25] These results were similar to the results obtained in this experiment, and we observed no significant difference in fluorescence properties before and after ligand exchange with Ami. (d) Photograph of Pt NCs in PBS buffer solution upon excitation with a 535 nm laser (left) and under ambient light (right). The Pt NC solution exhibited bright red fluorescence when excited by the 535 nm laser.

coordination bond formation occurred between polyamidoamine dendrimers with fifth-generation hydroxyl surface groups [PAMAM (G5-OH)] and Pt ions during pre-equilibration, followed by reduction with a large amount of fructose (Figure 1a). Moreover, it was shown that Pt NCs can generally emit brighter fluorescence than other metal nanomaterials, such as Au NCs.[8−12,16] Highly luminescent Pt NCs enable sensing and imaging of the targeted biomolecules in cells and living organism with low background and high sensitivity.

In terms of magnetism, Pt is typically paramagnetic in the bulk, whereas it was reported to show ferromagnetism in two-dimensional (2D) thin films, 1D monatomic chains, and 0D NCs. It was reported that a NC of 13 Pt atoms exhibits superparamagnetism without hysteresis.[26] However, to the best of our knowledge, there have been no reports of Pt NCs that have both fluorescent and ferromagnetic properties.

Here, we report new significant progress in the development of Pt NCs. We found that Pt NCs have coexistence of fluorescent and ferromagnetic properties and characterized these new multifunctional fluorescent-magnetic Pt NCs. The NCs are promising candidates for utilization as multimodal fluorescent-magnetic contrast agents in *in vitro* and *in vivo*

bioimaging applications, such as fluorescence microscopy and MRI, because of their ultrafine size, excellent photostability, modifiable surface structure and, more importantly, low toxicity. They may also be suitable as drug carriers to develop a magnetically guided traceable drug delivery approach for targeted therapy that will minimize collateral damage to normal tissues and allow tracking of the delivery and efficacy of the therapy.

2. EXPERIMENTAL SECTION

2.1. Materials. Hexachloroplatinic acid salt (H_2PtCl_6), Na_2HPO_4, NaH_2PO_4, NaOH, methanol, fructose, 4-aminobutyl acid (Ami) and 4-(4,6-dimethoxy-1,3,5-triazin-2-yl)-4-methylmorpholinium chloride (DMT-MM) were purchased from Wako (Japan). PAMAM dendrimers with fifth-generation hydroxyl surface groups (PAMAM (G5-OH)) were purchased from Sigma−Aldrich (Japan). Protein A was purchased from Thermo Fisher Scientific K. K (Japan). Anti-HER2 antibody (Herceptin) was purchased from CHUGAI Pharmaceutical Co. Ltd. (Japan). SK-BR-3 cells were purchased from ATCC (USA), and polylysine-coated glass bottom dish was purchased from Matsunami Glass Ind., Ltd. (Japan).

2.2. Instruments. The fluorescence of the synthesized Pt NCs was tested using a spectrofluorometer (FP-8200ST, JASCO Corp., Japan), and their absolute quantum yields (QYs) were evaluated using a quantum yield measurement system (C10027, Hamamatsu Photonics, Japan). The fluorescence lifetime was measured at room temperature with a picosecond fluorescence lifetime measurement system (C11200, Hamamatsu Photonics, Japan) with the second harmonic generation (532 nm) of a Nd/YAG laser (PL2231-50, Ekspla, Lithuania) as the excitation source. The high-performance liquid chromatography (HPLC) system consisted of a 500 μL sample loop, a pump (LC-20AD, Shimadzu, Japan), a UV/vis absorbance detector (SPD-20A, Shimadzu, Japan), and a fluorescence detector (RF-20A, Shimadzu, Japan). The TSKgel QAE-2SW anion-exchange HPLC column and TSKgel guard gel QAE-SW were purchased from TOSOH Corp (Japan). Atomic-resolution high-angle annular dark-field scanning transmission electron microscopy (HAADF-STEM) images were acquired using a JEM-ARM200F (JEOL, Japan). Confocal fluorescence imaging of SK-BR-3 cells was performed with an FV1000 instrument (Olympus). The magnetization vs magnetic field curves at 300 K for powdered [PtNC(Ami)] were measured with a magnetic property measurement system (MPMS 3, Quantum Design, Japan).

2.3. Synthesis of Pt NCs. Synthesis methods were carried out according to our previously published methods.[25] First, 0.25 μmol of PAMAM (G5-OH) was dissolved in 5.0 mL of Millipore water (18.2 MΩ) in an ice bath. Then, this PAMAM solution was mixed with H_2PtCl_6 (90 μL, 0.5 M). The reaction mixture was allowed to stand in the dark at 4 °C for 5 days to increase the incorporation of Pt ions into the dendrimers. After 5 days at pre-equilibration, fructose (2.25 mL, 2 M) was added as a reductant. The reduction was allowed to proceed at 90 °C for 2 weeks with continuous stirring to produce fluorescent Pt NCs. Large Pt colloidal nanoparticles were removed by ultracentrifugation (Optima MAX-TL, Beckman Coulter, Inc.; 100,000 G) for 30 min at 4 °C. A total of 1.5 mL of Ami (4 M) was added to 5 mL of Pt NC solution to maintain a molar ratio of Pt ion/Ami of 1:200 for ligand exchange.

After ligand exchange, anion-exchange chromatography was performed to purify [PtNC(Ami)]. For this process, 300 μL of [PtNC(Ami)] solution was loaded onto a QAE-anion-exchange column equilibrated with buffer A [30% methanol in phosphate buffer (20 mM, pH 7.5)]. The column was washed with 8 mL of phosphate buffer A, and then bound [PtNC(Ami)] was eluted with 12 mL of buffer B (30% methanol in phosphate buffer [20 mM, pH 7.5) containing NaCl (1 M)] at a flow rate of 0.8 mL/min. The detection wavelength for UV absorption was set to 275 nm. The monitored fluorescence wavelength was 620 nm, and the excitation wavelength was set to 535 nm. After this step, the column was washed again with 32 mL of buffer A.

2.4. Transmission Electron Microscopy. Pt NCs were diluted with methanol, dropped onto a grid (UHR-M10, STEM), dried, and observed with a JEOL JEM-ARM200F STEM operating at 200 kV using a CEOS aberration corrector for the probe-forming lens. For STEM imaging, the semiangle of beam convergence was set to 23 mrad. HAADF-STEM images with atomic resolution were acquired with detector semiangles of 68−170 mrad. For the NC size measurement, the NC regions in the HAADF-STEM images were manually filled, and the area was calculated using the "analyse particle" function of ImageJ. The NC size was defined as the diameter of a circle with the same area as the NC as measured manually from the HAADF-STEM image.

2.5. Fluorescence Lifetime. The fluorescence lifetime at room temperature was obtained with a picosecond fluorescence lifetime measurement system (C11200, Hamamatsu Photonics) with the second harmonic generation (532 nm) of a Nd/YAG laser (PL2231-50, Ekspla) as the excitation source. The fluorescence lifetime signals were collected in fluorescence channels between 580 and 680 nm, and the time resolution was 69 ps. The excitation intensity was approximately 0.16 J/cm^2 at 50 Hz.

2.6. Preparation of Pt Nanocluster Bionanoprobes. [PtNC(Ami)] was conjugated with ProteinA using a DMT-MM coupling reaction. To maintain antibody activity, ProteinA[23−25] was used as an adapter protein for the antibody. ProteinA can bind specifically to the Fc region of the antibody without blocking the antigen-binding site. First, [PtNC(Ami)] (25.0 μM, 400 μL) was mixed with DMT-MM (0.25 M, 400 μL) for 30 min at 25 °C, followed by ProteinA (100 μM, 325 μL) for 2 h at 25 °C. The molar ratio of [PtNC(Ami)]/ProteinA/DMT-MM was set to 1:3.25:10,000.

2.7. Confocal Fluorescence Microscopy. A culture dish containing SK-BR-3 cells was washed twice with PBS. Then, anti-HER2 antibody (10 μM, 800 μL) was added to the dish, which was then incubated for 10 min at 37 °C. After washing twice with PBS buffer, 100 μL of ProteinA-conjugated [PtNC(Ami)] was added to SK-BR-3 cells, and [PtNC(Ami)] was specifically bound to anti-HER2 antibody after 5 min incubation at 37 °C. Confocal fluorescence imaging was performed with an FV1000 instrument (Olympus) using an oil immersion objective lens (UPlanFLN, 60×, N.A. = 1.3, Olympus). The excitation laser wavelength was 515 nm.

2.8. Macroscopic Magnetometry. The magnetization-magnetic field ($M-H$) curves at 300 K for powdered [PtNC(Ami)] and MRI contrast agent gadolinium 3-diethylenetriamine pentaacetate-bis(methylamide) (Gd-HP-DO3A) were obtained with a magnetic property measurement system (MPMS-3, quantum design). The powdered sample was prepared by vacuum desolvation of the synthetic solvent in a vacuum desiccator for 1 day. The sample (mass: 16.81 mg) was packed in an Al foil bag (mass: 24.44 mg), and $M-H$ curve measurements were performed at 300 K. The obtained experimental data (in units of emu/g) were divided by mass of the sample after removing the background of those measured on Al foil alone. The reference sample Gd-HP-DO3A was purchased from Cosmo Bio Co., Ltd. (Japan).

3. RESULTS AND DISCUSSION

3.1. Evaluation of Optical Properties: Photoluminescence and Quantum Yields. Fluorescence intensity and photostability are fundamental features for probes to be used in biomedical applications to obtain well-defined images with a high signal-to-noise ratio and to perform long-time *in vivo* imaging. To eliminate autofluorescence from PAMAM dendrimers, the Pt NCs were subjected to ultracentrifugation and ligand exchange with Ami, which afforded [PtNC(Ami)] (Figure 1b); then, the [PtNC(Ami)] was purified via anion-exchange chromatography. Inductively coupled plasma mass spectrometry (ICP-MS) indicated that this washed sample included only Pt (2.83 mg/L). After collecting the washed [PtNC(Ami)], we recorded its excitation−emission matrix spectra with a spectrofluorophotometer, and the NCs showed bright red fluorescence (620 nm) upon 535 nm excitation
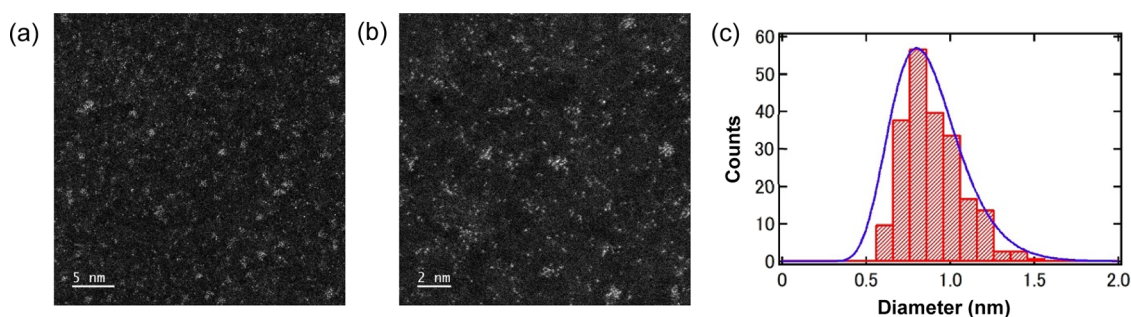
Figure 2. Morphology and Structural characterizations of Pt NCs. (a) HAADF-STEM micrograph at a magnification of 6 million, in which the pale areas represent Pt. Scale bar: 5 nm. (b) HAADF-STEM micrograph at a magnification of 12 million, in which the pale areas represent Pt. Scale bar: 2 nm. (c) Size histogram obtained from measurements of 206 NCs in the HAADF-STEM micrographs. The curve represents a log−normal distribution function. The mean NC diameter was 0.8 nm, and the standard deviation was 0.2 nm. These NCs were similar in size to the Pt NCs prepared in our previous work.[25]
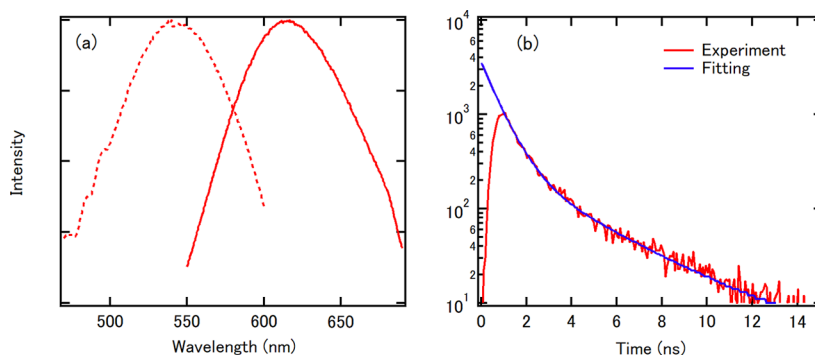
Figure 3. Fluorescence lifetime measurements of [PtNC(Ami)]. (a) Excitation (dashed line) and emission (solid line) spectra of [PtNC(Ami)] in water. This excitation energy of 532 nm corresponds to the absorption peak shown in Figure 3a. (b) The fluorescence decay curve of [PtNC(Ami)] with the corresponding fitted curve (an exponential function with two components).

(Figure 1c,d). In previously work, Pt NCs embedded in PAMAM (G5-OH) dendrimers also displayed red fluorescence with a maximum excitation/emission wavelength of 535/630 nm.[25] These results were similar to the results obtained in this study, and we observed no significant difference in fluorescence properties before and after ligand exchange with Ami.

Next, we evaluated the absolute *QYs* of the synthesized [PtNC(Ami)] using a quantum yield measurement system. *QY* is defined as $QY = PNem/PNab$, where PNem and PNab are the numbers of emitted and absorbed photons by the fluorescent particles, respectively. The *QY* for [PtNC(Ami)] was found to be 1.0% in water, while that for another infrared photoluminescent species, Au NCs (emission: 1000 nm) in water, was 0.6%.[10] Absolute *QY* measurements showed that the intensity of the red fluorescence of [PtNC(Ami)] matched that of Au NCs, which have been applied as probes for *in vivo* imaging, thus demonstrating the potential of our red-emitting Pt NCs for biomedical applications.

3.2. HAADF-STEM Imaging. HAADF-STEM images show dispersed [PtNC(Ami)] and Pt atoms with clear contrast (Figure 2a,b). This high contrast occurs because the atomic number contrast (Z-contrast) is proportional to Z^2, and the atomic number (Z) of Pt is large, at 78. Based on measurements of 206 NCs of [PtNC(Ami)], the diameter of the NCs was 0.8 ± 0.2 nm. The size distribution was found to be log−normal, as is common for samples of nanoparticle aggregates fabricated by vacuum deposition or sputtering (Figure 2c).[31] Then, this size histogram was also fitted with log−normal distribution function (1) and there was a very

satisfactory agreement between the experimental data and the theoretical curve. This demonstrated that the nanocluster size distribution properly followed a log−normal distribution function. Therefore, since [PtNC(Ami)] is smaller than other bioimaging nanomaterials such as QDs (2.0−10.0 nm) and Au NCs (1.9−5.0 nm),[10,12] our Pt NCs show promise as useful fluorescent probes for efficient protein labeling without evidently affecting their intrinsic physiological properties or targeting ability.

$$F(x) = 57e^{-\ln\left(\frac{x}{0.8}\right)/(0.345)^2}\dots \tag{1}$$

3.3. Fluorescence Lifetime. The fluorescence lifetime is the characteristic time for which a molecule remains in its excited state before returning to the ground state and is an intrinsic property of fluorescent probes and a signature of the targeted fluorophores. Figure 3a shows the excitation and emission spectra of [PtNC(Ami)] in water, showing maximum emission at 620 nm upon 535 nm excitation. The fluorescence lifetime of [PtNC(Ami)] was measured at room temperature using a fluorescence lifetime measurement system with the second harmonic generation (532 nm) of a Nd/YAG laser as the excitation source. This excitation energy of 532 nm corresponds to the absorption peak shown in Figure 3a. A semilogarithmic plot of the fluorescence intensity as a function of time, as shown in Figure 3b, decreases linearly with an inflection point at approximately 3 ns, which is defined as the sum of two exponential functions. The following equation was fit to the time-resolved fluorescence curve (Figure 3b)
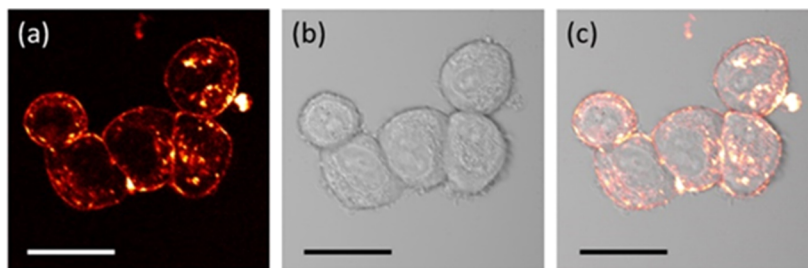
Figure 4. After incubation with Pt bionanoprobes: (a) confocal fluorescence image of SK-BR-3; (b) transmission image of SK-BR-3; (c) merged image of SK-BR-3. Scale bar = 30 μm.
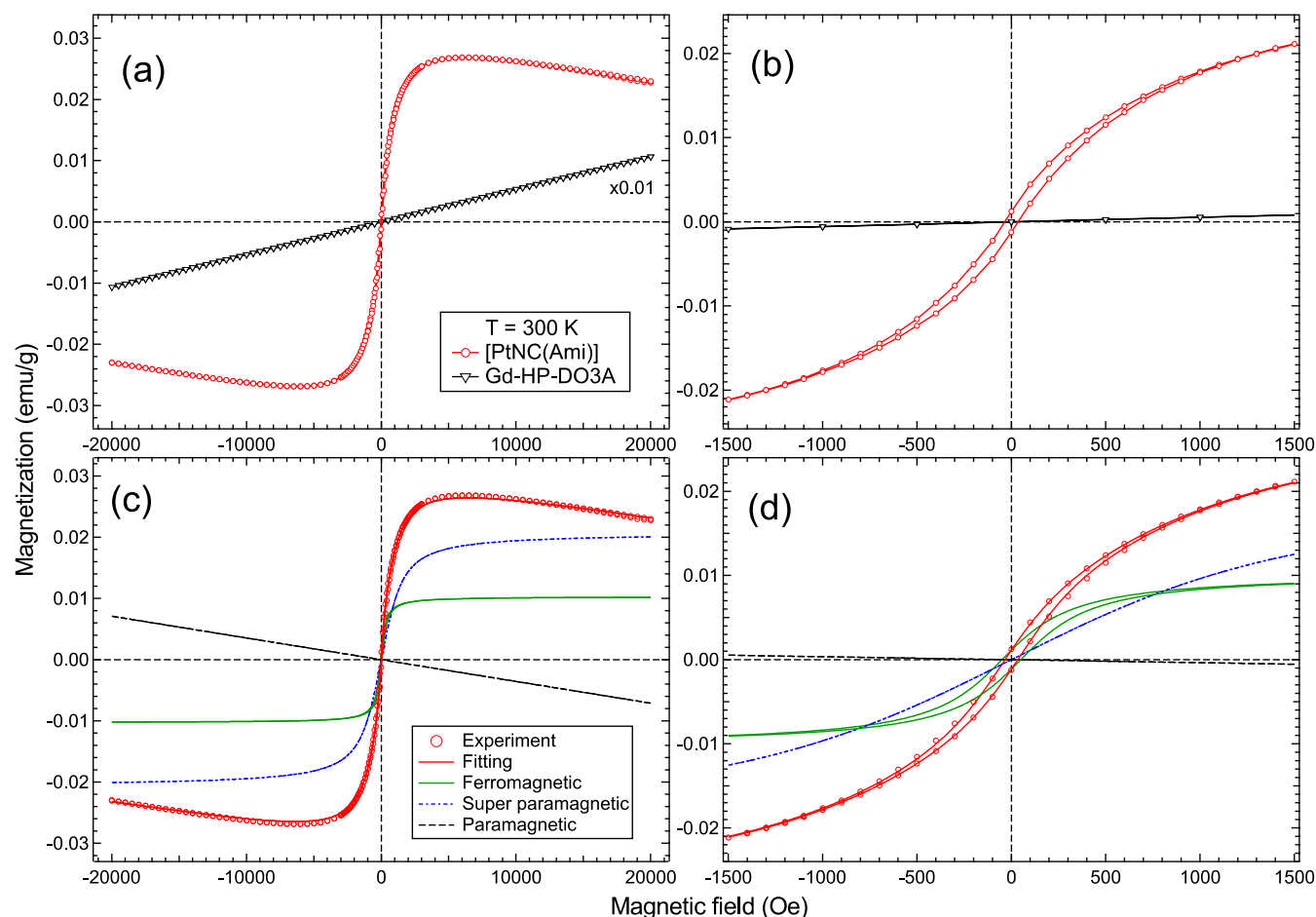
Figure 5. Magnetic characterization of Pt NCs at 300 K. (a) Magnetization vs magnetic field ($M{-}H$) curves of $[\mathrm{PtNC(Ami)}]$ (red) and MRI contrast agent Gd-HP-DO3A (black) between ± 20 kOe at 300 K. (b) Low-H limit of the $M{-}H$ curves of $[\mathrm{PtNC(Ami)}]$ (red) and Gd-HP-DO3A (black) at 300 K between ± 1.5 kOe. (c,d) Experimental data and magnetization curve fits, $M(H)$, as defined by eq 3 for $[\mathrm{PtNC(Ami)}]$ at 300 K between ± 20 kOe and ± 1.5 kOe, respectively. The $M(H)$ function contained ferromagnetic (green), superparamagnetic (blue), and paramagnetic (black) components.

$$I(t) = I_1 e^{-t/\tau_1} + I_2 e^{-t/\tau_2}\cdots \tag{2}$$

where $I(t)$ is the fluorescence intensity and I_1 and I_2 are the intensities of the first and second components, respectively. Since only one peak was observed in the histogram in the TEM image (Figure 2c), the synthesized Pt NCs were considered to be atomically monodispersed. Therefore, each nanoparticle emits photons via two processes with different time constants. From this fit, the lifetimes of $[\mathrm{PtNC(Ami)}]$ were determined to be $\tau_1 = 0.73$ ns and $\tau_2 = 3.4$ ns. To consider the source for this fluorescent behavior, we compared our results to those from red-emitting (620 nm) Ru-ligand complexes.[32] These Ru-

ligand complexes exhibited a lifetime of several hundred nanoseconds, much longer than that of $[\mathrm{PtNC(Ami)}]$, and their fluorescence was attributed to metal-to-ligand charge transfer (MLCT). Therefore, the nanosecond-range fluorescence lifetime of $[\mathrm{PtNC(Ami)}]$ indicates that the fluorescence emission is independent of the ligands and instead is the result of intraband or interband transmission inside the metal core.

3.4. *In Vitro* Imaging of HER2. To demonstrate the applicability of $[\mathrm{PtNC(Ami)}]$ as a bionanoprobe, the Pt bionanoprobe (ProteinA conjugated $[\mathrm{PtNC(Ami)}]$) was then applied to image HER2 in SK-BR-3 cells, a HER2 overexpressing breast cancer cell line.[33,34] SK-BR-3 cells were

incubated with anti-HER2 antibody, followed by staining HER2 with Pt bionanoprobes. Figure 4a−c show the confocal laser scanning microscopy images of SK-BR-3 cells and we observed red fluorescence from Pt bionanoprobes at the cellular surface, indicating that they specifically bound to HER2 via anti-HER2 antibody. These results demonstrated that our Pt bionanoprobe bound to HER2-overexpressing SK-BR-3 cells with a greater affinity and higher selectivity.

3.5. Magnetic Characterization. To investigate the coexistence of magnetism and red luminescence, we performed macroscopic magnetometry measurements. The $M-H$ curves of $[PtNC(Ami)]$ and Gd-HP-DO3A at 300 K with a magnetic field range between ± 20 kOe were obtained (Figure 5a). Gd-HP-DO3A was analyzed for comparison because it is a common MRI contrast agent. The $M-H$ curve of Gd-HP-DO3A is characteristic of paramagnetic behavior, whereas the $M-H$ curve of $[PtNC(Ami)]$ shows primarily superparamagnetic (SPM) behavior but also contains a linear paramagnetic component at high-H limits (>1500 Oe). In the low-H range (<1500 Oe in Figure 5b) hysteresis is observed at 300 K, indicating the presence of a ferromagnetic component (FM) in $[PtNC(Ami)]$, as well.

To extract the FM, SPM, and paramagnetic components from the obtained $M-H$ curve, a magnetization curve fit, $M(H)$, was applied as follows[35−37]

$$M(H) = \frac{2M_{\mathrm{FM}}}{\pi}\tan^{-1}\left[\frac{H \pm H_{\mathrm{c}}}{H_{\mathrm{c}}}\tan\left(\frac{\pi S}{2}\right)\right]$$
$$+ M_{\mathrm{SPM}}\left[\coth^{-1}\left(\frac{\overline{\mu}H}{k_{\mathrm{B}}T}\right) - \left(\frac{\overline{\mu}H}{k_{\mathrm{B}}T}\right)^{-1}\right] + \chi H \cdots$$
$$(3)$$

Here, k_{B} is the Boltzmann constant, T is the temperature, and H is the magnetic field. The first, second, and third terms correspond to the FM, SPM, and paramagnetic components, respectively. M_{FM} and M_{SPM} represent the saturation magnetization of the FM and SPM components. H_{c} and S in the FM term are the coercive field and the ratio of the remanent magnetization to M_{FM}. $\overline{\mu}$ in the SPM term is the average moment of SPM. We found, as shown in Figure 5c,d, that the $M(H)$ fitting result completely reproduced the experimental $M-H$ curve when $M_{\mathrm{FM}} = 1.03 \times 10^{-2}$ (emu/g), $M_{\mathrm{SPM}} = 2.07 \times 10^{-2}$ (emu/g), and $H_{\mathrm{c}} = 50$ Oe. The obtained values of M_{FM} and M_{SPM} are the same order of magnitude as those of previously reported Pt NCs without hysteresis.[26] In Pt, the surface effect dominates when the size is reduced to form thin films or nanoclusters. At the surface, the effect of the crystal field becomes smaller, resulting in a magnetic high-spin state. Therefore, we conclude that the realization of a high-spin state in Pt is the key to realizing this magnetism. Compared to those in previous reports, our Pt NCs are novel in that they exhibit both fluorescence and magnetism at room temperature.

4. CONCLUSIONS

In summary, we successfully synthesized novel multifunctional fluorescent-magnetic Pt NCs with a diameter of 0.8 ± 0.2 nm. These Pt NCs exhibited high fluorescence intensity (excitation: 535 nm, emission: 620 nm) and ferromagnetic behavior. Their known photostability and biocompatibility[23−25] mean that they also have potential as bioimaging probes for acquiring fluorescence images and performing MRI (See Figure S1 in Supporting Information). Furthermore, a combination of optical and magnetic properties in a single material would enable the simultaneous fluorescence imaging/magnetic separation of target cells or exosomes from clinical samples such as blood and controlled photorelease/magnetically targeting during drug delivery. Overall, this work opens new possibilities for the rational design and development of effective and safe multimodal nanosystems in other biomedical applications.

■ ASSOCIATED CONTENT

ⓢ Supporting Information

The Supporting Information is available free of charge at https://pubs.acs.org/doi/10.1021/acsomega.4c06765.

T1-weighted MR images of $[PtNC(Ami)]$ (PDF)

■ AUTHOR INFORMATION

Corresponding Author

Shin-ichi Tanaka − *National Institute of Technology, Kure College, Kure, Hiroshima 737-8506, Japan;* ◉ orcid.org/0000-0002-5242-1355; Email: s-tanaka@kure-nct.ac.jp

Authors

Kohei Yamagami − *Japan Synchrotron Radiation Research Institute (JASRI), Sayo-cho, Hyogo 679-5198, Japan*

Kazuhisa Sato − *Research Center for Ultra-High Voltage Electron Microscopy, Osaka University, Ibaraki, Osaka 567-0047, Japan; Division of Materials and Manufacturing Science, Graduate School of Engineering, Osaka University, Osaka 565-0871, Japan;* ◉ orcid.org/0000-0001-9078-2541

Hidehiro Yasuda − *Research Center for Ultra-High Voltage Electron Microscopy, Osaka University, Ibaraki, Osaka 567-0047, Japan; Division of Materials and Manufacturing Science, Graduate School of Engineering, Osaka University, Osaka 565-0871, Japan;* ◉ orcid.org/0000-0002-9877-9803

Hirohiko Niioka − *Graduate School of Information Science and Technology, Osaka University, Osaka 565-0871, Japan*

Hiroki Wadati − *Department of Material Science, Graduate School of Science, University of Hyogo, Ako-gun, Hyogo 678-1297, Japan; Institute of Laser Engineering, Osaka University, Osaka 565-0871, Japan;* ◉ orcid.org/0000-0001-5969-8624

Complete contact information is available at:
https://pubs.acs.org/10.1021/acsomega.4c06765

Author Contributions

The manuscript was written through contributions of all authors. All authors have given approval to the final version of the manuscript.

Notes

The authors declare no competing financial interest.

ACKNOWLEDGMENTS

REFERENCES

(1) Meng, L.; Ma, X.; Jiang, S.; Ji, G.; Han, W.; Xu, B.; Tian, J.; Tian, W. High-efficiency fluorescent and magnetic multimodal probe for long-term monitoring and deep penetration imaging of tumours. *J. Mater. Chem. B* **2019**, *7*, 5345−5351.

(2) Serrano García, R.; Stafford, S.; Gun'ko, Y. K. Recent Progress in Synthesis and Functionalization of Multimodal Fluorescent-Magnetic Nanoparticles for Biological Applications. *Appl. Sci.* **2018**, *8*, 172.

(3) Banerjee, T.; Tummala, T.; Elliott, R.; Jain, V.; Brantley, W.; Hadorn, L.; Santra, S. Multimodal Magneto-Fluorescent Nanosensor for Rapid and Specific Detection of Blood-Borne Pathogens. *ACS Appl. Nano Mater.* **2019**, *2*, 5587−5593.

(4) Corr, S. A.; Rakovich, Y. P.; Gun'ko, Y. K. Multifunctional Magnetic-fluorescent Nanocomposites for Biomedical Applications. *Nanoscale Res. Lett.* **2008**, *3*, 87.

(5) Jańczewski, D.; Zhang, Y.; Das, G. K.; Yi, D. K.; Padmanabhan, P.; Bhakoo, K. K.; Tan, T. T. Y.; Selvan, S. T. Bimodal Magnetic-Fluorescent Probes for Bioimaging. *Microsc. Res. Tech.* **2011**, *74*, 563−576.

(6) Ma, J.-J.; Yu, M.-X.; Zhang, Z.; Cai, W.-G.; Zhang, Z.-L.; Zhu, H.-L.; Cheng, Q.-Y.; Tian, Z.-Q.; Pang, D.-W. Gd-DTPA-coupled Ag$_2$Se quantum dots for dual-modality magnetic resonance imaging and fluorescence imaging in the second near-infrared window. *Nanoscale* **2018**, *10*, 10699−10704.

(7) McAdams, S. G.; Lewis, D. J.; McNaughter, P. D.; Lewis, E. A.; Haigh, S. J.; O'Brien, P.; Tuna, F. High magnetic relaxivity in a fluorescent CdSe/CdS/ZnS quantum dot functionalized with MRI contrast molecules. *Chem. Commun.* **2017**, *53*, 10500−10503.

(8) Zheng, J.; Zhang, C.; Dickson, R. M. Highly Fluorescent, Water-Soluble, Size-Tunable Gold Quantum Dots. *Phys. Rev. Lett.* **2004**, *93*, 077402.

(9) Zheng, J.; Petty, J. T.; Dickson, R. M. High Quantum Yield Blue Emission from Water-Soluble Au$_8$ Nanodots. *J. Am. Chem. Soc.* **2003**, *125*, 7780−7781.

(10) Chen, Y.; Montana, D. M.; Wei, H.; Cordero, J. M.; Schneider, M.; Le Guével, X.; Chen, O.; Bruns, O. T.; Bawendi, M. G. Shortwave Infrared in Vivo Imaging with Gold Nanoclusters. *Nano Lett.* **2017**, *17*, 6330−6334.

(11) Le Guével, X.; Wegner, K. D.; Würth, C.; Baulin, V. A.; Musnier, B.; Josserand, V.; Resch-Genger, U.; Coll, J.-l. Tailoring the SWIR emission of gold nanoclusters by surface ligand rigidification and their application in 3D bioimaging. *Chem. Commun.* **2022**, *58*, 2967−2970.

(12) Song, X.; Zhu, W.; Ge, X.; Li, R.; Li, S.; Chen, X.; Song, J.; Xie, J.; Chen, X.; Yang, H. A New Class of NIR-II Gold Nanocluster-Based Protein Biolabels for In Vivo Tumor-Targeted Imaging. *Angew. Chem., Int. Ed.* **2021**, *60*, 1306−1312.

(13) Román-Velázquez, C. E.; Noguez, C.; Garzón, I. L. Circular Dichroism Simulated Spectra of Chiral Gold Nanoclusters: A Dipole Approximation. *J. Phys. Chem. B* **2003**, *107*, 12035−12038.

(14) Gautier, C.; Bürgi, T. Chiral Inversion of Gold Nanoparticles. *J. Am. Chem. Soc.* **2008**, *130*, 7077−7084.

(15) Santiago González, B.; Rodríguez, M. J.; Blanco, C.; Rivas, J.; López-Quintela, M. A.; Martinho, J. M. G. One Step Synthesis of the Smallest Photoluminescent and Paramagnetic PVP-Protected Gold Atomic Clusters. *Nano Lett.* **2010**, *10*, 4217−4221.

(16) Yu, F.; Xiang, H.; He, S.; Zhao, G.; Cao, Z.; Yang, L.; Liu, H. Gold nanocluster-based ratiometric fluorescent probe for biosensing of Hg^{2+} ions in living organisms. *Analyst* **2022**, *147*, 2773−2778.

(17) Richards, C. I.; Choi, S.; Hsiang, J.-C.; Antoku, Y.; Vosch, T.; Bongiorno, A.; Tzeng, Y.-L.; Dickson, R. M. Oligonucleotide-Stabilized Ag Nanocluster Fluorophores. *J. Am. Chem. Soc.* **2008**, *130*, 5038−5039.

(18) Cerretani, C.; Kanazawa, H.; Vosch, T.; Kondo, J. Crystal structure of a NIR-Emitting DNA-Stabilized Ag$_{16}$ Nanocluster. *Angew. Chem., Int. Ed.* **2019**, *58*, 17153−17157.

(19) Udaya Bhaskara Rao, T.; Pradeep, T. Luminescent Ag$_7$ and Ag$_8$ Clusters by Interfacial Synthesis. *Angew. Chem., Int. Ed.* **2010**, *49*, 3925−3929.

(20) Wei, W.; Lu, Y.; Chen, W.; Chen, S. One-Pot Synthesis, Photoluminescence, and Electrocatalytic Properties of Subnanometer-Sized Copper Clusters. *J. Am. Chem. Soc.* **2011**, *133*, 2060−2063.

(21) Kawasaki, H.; Kosaka, Y.; Myoujin, Y.; Narushima, T.; Yonezawa, T.; Arakawa, R. Microwave-assisted polyol synthesis of copper nanocrystals without using additional protective agents. *Chem. Commun.* **2011**, *47*, 7740−7742.

(22) Hyotanishi, M.; Isomura, Y.; Yamamoto, H.; Kawasaki, H.; Obora, Y. Surfactant-free synthesis of palladium nanoclusters for their use in catalytic cross-coupling reactions. *Chem. Commun.* **2011**, *47*, 5750−5752.

(23) Tanaka, S.; Miyazaki, J.; Tiwari, D. K.; Jin, T.; Inouye, Y. Fluorescent Platinum Nanoclusters: Synthesis, Purification, Characterization, and Application to Bioimaging. *Angew. Chem., Int. Ed.* **2011**, *50*, 431−435.

(24) Tanaka, S.; Aoki, K.; Muratsugu, A.; Ishitobi, H.; Jin, T.; Inouye, Y. Synthesis of green-emitting Pt$_8$ nanoclusters for biomedical imaging by pre-equilibrated Pt/PAMAM (G4-OH) and mild reduction. *Opt. Mater. Express* **2013**, *3*, 157−165.

(25) Tanaka, S.; Wadati, H.; Sato, K.; Yasuda, H.; Niioka, H. Red-Fluorescent Pt Nanoclusters for Detecting and Imaging HER2 in Breast Cancer Cells. *ACS Omega* **2020**, *5*, 23718−23723.

(26) Roduner, E.; Jensen, C. Magnetic Properties and the Superatom Character of 13-Atom Platinum Nanoclusters. *Magnetochemistry* **2015**, *1*, 28−44.

(27) Zhang, Z.; Chen, Y.; Zhou, L.; Chen, C.; Han, Z.; Zhang, B.; Wu, Q.; Yang, L.; Du, L.; Bu, Y.; Wang, P.; Wang, X.; Yang, H.; Hu, Z. The simplest construction of single-site catalysts by the synergism of micropore trapping and nitrogen anchoring. *Nat. Commun.* **2019**, *10*, 1657.

(28) Imaoka, T.; Akanuma, Y.; Haruta, N.; Tsuchiya, S.; Ishihara, K.; Okayasu, T.; Chun, W.-J.; Takahashi, M.; Yamamoto, K. Platinum clusters with precise numbers of atoms for preparative-scale catalysis. *Nat. Commun.* **2017**, *8*, 688.

(29) Witham, C. A.; Huang, W.; Tsung, C.-K.; Kuhn, J. N.; Somorjai, G. A.; Toste, F. D. Converting homogeneous to heterogeneous in electrophilic catalysis using monodisperse metal nanoparticles. *Nat. Chem.* **2010**, *2*, 36−41.

(30) Yamamoto, K.; Imaoka, T.; Chun, W.-J.; Enoki, O.; Katoh, H.; Takenaga, M.; Sonoi, A. Size-specific catalytic activity of platinum clusters enhances oxygen reduction reactions. *Nat. Chem.* **2009**, *1*, 397−402.

(31) Granqvist, C. G.; Buhrman, R. A. Ultrafine metal particles. *J. Appl. Phys.* **1976**, *47*, 2200−2219.

(32) Yoshikawa, N.; Kimura, H.; Yamabe, S.; Kanehisa, N.; Inoue, T.; Takashima, H. Emission property and DFT calculation for the ^{3}MLCT luminescence of $Ru(bpy)_2(L)^{2+}$ complex. *J. Mol. Struct.* **2016**, *1117*, 49−56.

(33) Fehling-Kaschek, M.; Peckys, D. B.; Kaschek, D.; Timmer, J.; Jonge, N. d. Mathematical modeling of drug-induced receptor internalization in the HER2-positive SKBR3 breast cancer cell line. *Sci. Rep.* **2019**, *9*, 12709.

(34) Seo, H.-S.; Ku, J. M.; Choi, H.-S.; Woo, J.-K.; Jang, B.-H.; Go, H.; Shin, Y. C.; Ko, S.-G. Apigenin induces caspase-dependent apoptosis by inhibiting signal transducer and activator of transcription 3 signaling in HER2-overexpressing SKBR3 breast cancer cells. *Mol. Med. Rep.* **2015**, *12*, 2977−2984.

(35) Stearns, M. B.; Cheng, Y. Determination of para-and ferromagnetic components of magnetization and magnetoresistance of granular Co/Ag films (invited). *J. Appl. Phys.* **1994**, *75*, 6894−6899.

(36) Ahmed, A.; Siddique, M. N.; Ali, T.; Tripathi, P. Defect assisted improved room temperature ferromagnetism in Ce doped SnO_2 nanoparticles. *Appl. Surf. Sci.* **2019**, *483*, 463−471.

(37) Sakamoto, S.; Nonaka, Y.; Ikeda, K.; Chi, Z.; Wan, Y.; Suzuki, M.; Fujimori, A.; Anh, L. D.; Hai, P. N.; Takeda, Y.; Saitoh, Y.; Kobayashi, M.; Tanaka, M.; Wakabayashi, Y. K.; Yamagami, H. Magnetization process of the insulating ferromagnetic semiconductor (Al,Fe)Sb. *Phys. Rev. B* **2020**, *101*, 075204.